Supplementary Information (SI) for Journal of Materials Chemistry C.

Supporting Information

Extreme Ultraviolet induced reactions of tin-oxo cage photoresists

Najmeh Sadegh,[a‡] Jarich Haitjema,[a‡] Yu Zhang,[a] Lianjia Wu,[a] Olivier Lugier,[a] Ivan Bespalov[a], Dimitrios Kazazis,[b] Michaela Vockenhuber,[b] Yasin Ekinci,[b] Katharina Witte,[b] Benjamin Watts,[b] Ivan Pollentier,[c] Danilo De Simone,[c] Albert M. Brouwer[a,d*]

[a]Advanced Research Center for Nanolithography, P.O. Box 93019, 1090 BA Amsterdam, The Netherlands

[b] PSI Center for Photon Science, Paul Scherrer Institute, Villigen PSI 5232, Switzerland

[c] Imec, Kapeldreef 75, B3001 Leuven, Belgium

[d] University of Amsterdam, van 't Hoff Institute for Molecular Sciences, P.O. Box 94157, 1090 GD Amsterdam, The Netherlands

Table of Contents

Additional experimental details

Synthesis. Tin-oxo cage materials were prepared as described before.[1] The tin-oxo cage was synthesized with tosylate counterions, after which the material was converted to hydroxide form (TinOH) by ion exchange using aqueous tetramethyl ammonium hydroxide.[2] The tin-oxo cage in its trifluoroacetate form (TinF) was prepared by reacting TinOH with two molar equivalents of trifluoroacetic acid.[3, 4]

Sample preparation. For x-ray absorption measurements the tin-oxo cage materials were spin coated onto 7.5 × 7.5 mm^2 substrates obtained from Norcada, composed of a silicon nitride (SiN_x) membrane covering a silicon substrate, with a 3 × 3 mm^2 window of freestanding silicon nitride (thickness *d* = 30 nm) in the middle. Spin coating of tin-oxo cage materials was performed using either a Suss Delta 10 or Chemat Technology Inc. Spin Master 50 spin coater. Spin coating was performed at 2500 rpm for 35 s, using a 20 mg/mL solution of TinOH or TinF in toluene. The solutions were filtered using a 0.2 μm PTFE filter prior to the spin coating. A post application bake of 30 s at 90°C was performed. The resulting thicknesses were ~40 nm (TinOH) and ~60 nm (TinF).

Reference samples for STXM were prepared as follows: a layer of polymethyl methacrylate (PMMA, average MW ~100.000 Da) or polystyrene (PS, average MW ~100.000 Da) was prepared by spin coating glass cover slips with these materials, using a Chemat Technology Inc. Spin Master 50 spin coater. The spin coated films were removed from the glass substrates using a water bath. Parts of the spin coated layer were picked up and placed on Si/SiN_x substrates (Silson, frame size: 5 × 5 mm^2, window size 1 × 1 mm^2, membrane thickness 100 nm). Flakes of PMMA/PS (thickness 77 nm and 240 nm, respectively) were made to partially cover the SiN_x window. Ultra-thin tin (Sn) flakes in metallic (β) form were prepared by microtoming from a tin wire (99.999%, 0.5 mm diameter, Sigma Aldrich) using a Leica Ultracut EM UC7 microtome set at a cutting thickness of 150 nm, leading to tin flakes of ~180 nm. These were picked up using the Si/SiN_x substrates mentioned above.

For EUV exposures and outgassing experiments at Imec, TinOH and TinF were spin-coated on 4 inch or 8 inch Si wafers. The wafers were pre-treated by heating up to 150 °C, covered with pure hexamethyldisilazane (HMDS) to form a single silane layer on the wafers followed by spinning them at 4000 rpm to remove the remaining HMDS. The treated wafers were heated again at 150 °C for 1 minute. A 10 mg/ml solution of TinF or TinOH was prepared in toluene and filtered using a 0.2 μm pore size syringe filter. For outgassing measurements, fresh solutions of TinOH and TinF were spin-coated at 2500 rpm for 30 seconds on top of the HMDS layer and then they were baked at 90 °C for 1 minute. The exposed wafers were developed using a mixture of isopropanol: water (2:1) for 30 seconds and then rinsed in pure water and dried under a flow of nitrogen.

Atomic Force Microscopy. The sample thickness *d* was measured using atomic force microscopy (AFM) for both reference and tin-oxo cage samples. The AFM tip was scanned across an edge of the material with the bare SiN_x membrane. For EUV-exposed materials, a corner of the exposed area was scanned. The scans were performed for both exposed non-developed material (see Fig. S1A as an example) and exposed and developed material (see Fig. S1B). For an exposed but not developed sample, the EUV exposed part will generally have a smaller film thickness, as a result of outgassing of volatile compounds. For an exposed developed sample, the non-exposed part will be dissolved by the developer, while the exposed part has been (at least partially) converted into insoluble material, which means it will remain on the substrate.

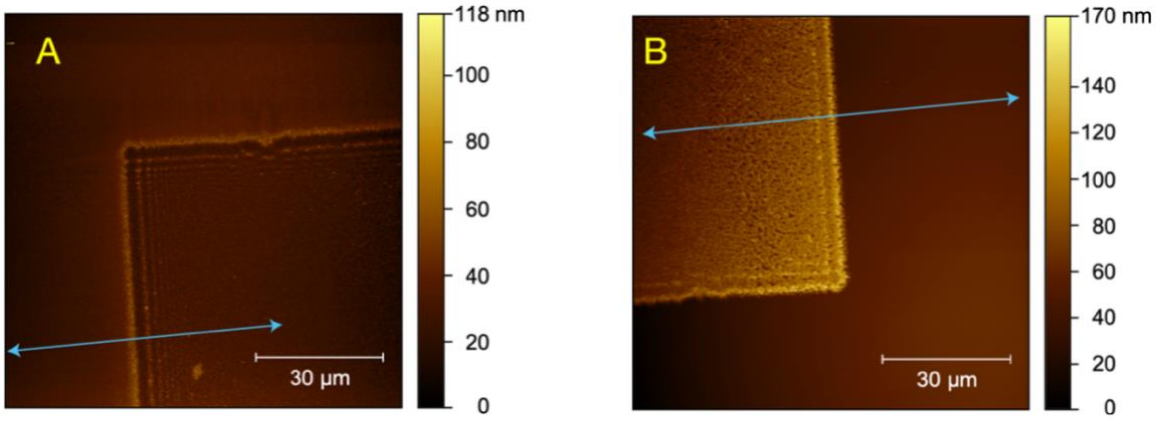

Fig. S1. AFM image of TinF spin coated on SiN_x, locally exposed (0.5 × 0.5 mm^2) to 150 mJ cm^{-2} of EUV irradiation. Non-developed (A) and developed using a 2:1 mixture of IPA/H_2O (B). Examples of cross sections are shown as light blue arrows.

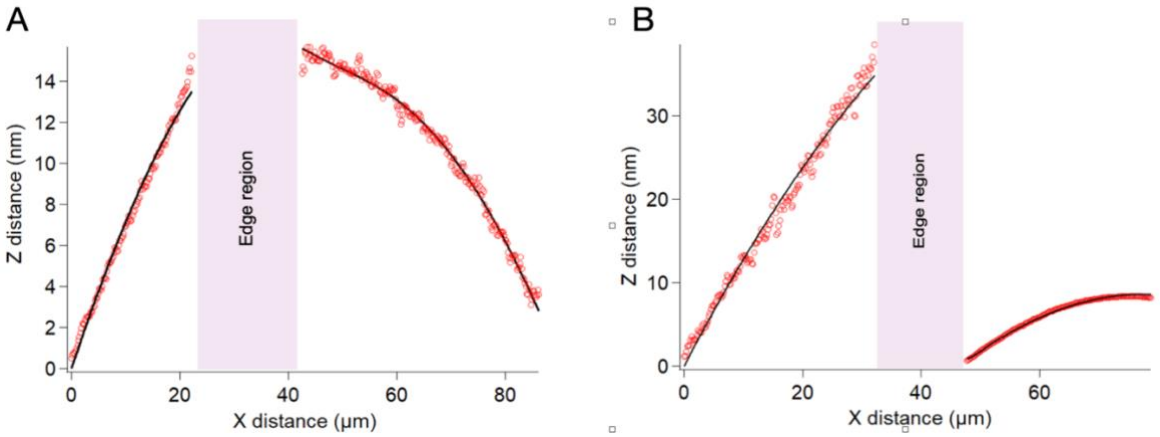

Fig. S2. Cross sections of the AFM images on TinF (Fig. S1) taken perpendicular to the exposure edge area, masking the edge region (pink rectangle). Open circles: experimental results, black lines: fit using bent step function. Fitted thickness loss (A): 5.7 ± 0.4 nm. Fitted remaining thickness (B): 44.6 nm ± 0.3 nm.

The film thickness can be extracted from Fig. S1 by taking cross sections perpendicular to the edge of the square. The step height can be calculated by fitting the cross section to a step function, described by Eq. S1.

$$f(x) = y_0 + \frac{h}{2}\tanh(\xi/w) + \alpha\xi + \beta\xi^2, \xi = x - x_0 \qquad \text{(S1)}$$

In eq. S1 y_0 is the vertical offset, h is the step height and x_0 is the x position of the step's inflection point. As is apparent from Fig. S2, AFM images have some inherent drift in the z signal, which is corrected for by the terms $\alpha\xi$ and $\beta\xi^2$. The fitting procedure was carried out using the open-source Gwyddion software, in which the bent step function is built-in.[5]
The flood exposures have dose fluctuations at the edges due to the knife-edge effect.[6] Therefore, this edge was masked in the fitting procedure (see Fig. S2). The same was done for the reference samples. Removing these data from the fitting procedure has the additional advantage that the result is independent on the type of step function that is chosen.
For reference samples (PS, PMMA, Sn) the edge between the flake and bare SiN_x was measured. The same procedure using a bent step function was applied.

X-ray absorption. Measurements were made using the Scanning Transmission X-ray Microscope (STXM) at the PolLux beamline[7] of the Paul Scherrer Institute, as described in our previous work.[8-10] Samples were prepared as described above. On each 3 × 3 mm^2 SiN_x window, nine squares of 500 × 500 μm^2 were irradiated with 92 eV photons at the XIL-II beamline.[11] Some samples were analyzed after exposure only, others were developed with isopropanol/water 2:1 for 35 seconds. To identify the squares, the one in the center was displaced by 100 µm from the center of the 3 × 3 array. For all measurements, the beam was defocused to a spot of ~1 µm by moving the sample ~100 µm out of focus. By measuring the NEXAFS at the C-edge for TinOH and TinF with different dwell times we could show that this effectively reduced the radiation damage to a negligible level.

Images (150 × 150 μm^2; 300 × 150 or 150 × 150 pixels) were recorded at 320, 515 and 550 eV by scanning lines across the edges between exposed and unexposed areas, using a dwell time of 12 µs. It is important to record the data for exposed and unexposed areas with minimal real-time difference, to avoid effects of fluctuation of the light intensity, which is visible upon close inspection of the example data in Fig. 2 in the main text.

Carbon K-edge spectra of PS and PMMA and the tin $M_{4,5}$ edge of the tin sample were measured by scanning lines of 25 µm across the sample and reference areas, with a dwell time of 100 ms.

STXM data processing. The absorbance images recorded at three energies give rise to three equations with the (relative) concentrations *c* of the elements as the unknowns, and a common thickness *d*. See eq. S2.

$$\begin{aligned} A_{320} &= \alpha_{320} \cdot d = (c_C\sigma_{C(320)} + c_O\sigma_{O(320)} + c_{Sn(320)}\sigma_{Sn(320)}) \cdot d \\ A_{515} &= \alpha_{515} \cdot d = (c_C\sigma_{C(515)} + c_O\sigma_{O(515)} + c_{Sn(515)}\sigma_{Sn(515)}) \cdot d \\ A_{550} &= \alpha_{550} \cdot d = (c_C\sigma_{C(550)} + c_O\sigma_{O(550)} + c_{Sn(550)}\sigma_{Sn(550)}) \cdot d \end{aligned} \quad \text{(S2)}$$

In Eq. S1, α_E is the total absorption coefficient at energy *E* in cm^{-1}, *d* is the film thickness in cm, c_X is the concentration of element X in mol cm^{-3} and $\sigma_{X(E)}$ is the absorption cross section (cm^2 mol^{-1}) of element X at energy *E*. Because *d* is constant within the same absorption measurement, the set of equations can be solved for the three unknowns c_C, c_O and c_{Sn} by converting it to a matrix form (eq. S3).

$$\begin{pmatrix} A_{320} \\ A_{515} \\ A_{550} \end{pmatrix} = d \begin{pmatrix} \sigma_{C(320)} & \sigma_{O(320)} & \sigma_{Sn(320)} \\ \sigma_{C(515)} & \sigma_{O(515)} & \sigma_{Sn(515)} \\ \sigma_{C(550)} & \sigma_{O(550)} & \sigma_{Sn(550)} \end{pmatrix} \begin{pmatrix} c_C \\ c_O \\ c_{Sn} \end{pmatrix} \quad \text{(S3)}$$

The solution of eq. S3 is given by eq. S4.

$$\begin{pmatrix} c_C \\ c_O \\ c_{Sn} \end{pmatrix} d = \begin{pmatrix} \sigma_{C(320)} & \sigma_{O(320)} & \sigma_{Sn(320)} \\ \sigma_{C(515)} & \sigma_{O(515)} & \sigma_{Sn(515)} \\ \sigma_{C(550)} & \sigma_{O(550)} & \sigma_{Sn(550)} \end{pmatrix}^{-1} \begin{pmatrix} A_{320} \\ A_{515} \\ A_{550} \end{pmatrix} \quad \text{(S4)}$$

The solution contains the concentrations of each element multiplied by the film thickness *d*, which is the surface density *S* in mol cm^{-2}. If *d* is known (AFM measurements), the concentration of the element in mol cm^{-3} can be easily obtained through division by *d*. However, reporting the values in mol cm^{-2} has the advantage that different EUV doses can be conveniently compared. This is because the surface density is unaffected by densification of

the material. The values in in mol cm^{-2} can therefore easily be compared to study losses or gains of elements. In contrast, elemental density values in in mol cm^{-3} depend on both compression of the material and elemental gain or loss; they are therefore less straightforward to interpret.

The elemental cross sections $\sigma_{X(E)}$ at selected energies can be approximated by tabulated values such as those by Chantler,[12, 13] who uses a purely computational approach, or by Henke and coworkers[14] who use a combination of computation and experimental results. The elemental cross sections were also independently measured, as will be described below.

STXM raster scans inherently contain photon noise. As an estimate for the statistical error within the measurements, the standard error of the mean (SEM, $s_{\bar{x}}$) can be used, which is given by $s/\sqrt{N}$ (in which s is the standard deviation and N the number of measurements, in this case the number of pixels). This can be calculated from the standard deviations in pixel intensity of the studied area. From this, the SEM of other measured variables can be calculated. The standard error of the mean propagates in the same way as the standard deviation, as is given by the well-known "propagation of errors" formula eq. S5.

$$s_f = \sqrt{\left(\frac{\partial f}{\partial x}\right)^2 s_x^2 + \left(\frac{\partial f}{\partial y}\right)^2 s_y^2 + \left(\frac{\partial f}{\partial z}\right)^2 s_z^2 + \dots} \qquad \text{(S5)}$$

in which s_f represents the standard deviation of the function f, s_x represents the standard deviation of x, s_y represents the standard deviation of y, and so forth.[15] In this formula, the standard deviation can be replaced by the SEM by substituting s_x with $s_x N_x^{-1/2} = s_{\bar{x}}$, where N_x is the number of measurements on variable x (for example the number of pixels in the image area under study) and $s_{\bar{x}}$ is the SEM. Using Eq. S5 we can obtain the SEM for all measured quantities. For example, the SEMs of the absorption values are given by eq. S6:

$$s_{\bar{A}} = \sqrt{\left(\frac{\partial A}{\partial \bar{I}}\right)^2 s_{\bar{I}}^2 + \left(\frac{\partial A}{\partial \bar{I}_0}\right)^2 s_{\bar{I}_0}^2} \qquad \text{(S6)}$$

Using $A = -\ln(\bar{I}/\bar{I}_0)$ and taking the derivative, we obtain eq. S6:

$$s_{\bar{A}} = \sqrt{\left(-\frac{1}{\bar{I}}\right)^2 s_{\bar{I}}^2 + \left(\frac{1}{\bar{I}_0}\right)^2 s_{\bar{I}_0}^2} \qquad \text{(S7)}$$

The SEMs of the elemental densities (or loss of elemental densities in case of a non-developed sample) were calculated using Eq. S5, replacing all due quantities. These are the statistical errors in the STXM measurements and the errors in the absorption cross section at each photon energy.

For the cross sections, both experimental and tabulated values were used. For tabulated values, the error in σ was neglected because it is not known. For the experimentally obtained values, the SEM was calculated using Eq. S8.

$$s_{\bar{\sigma}_{E,X}} = \frac{s_{\bar{A},E}}{\rho_X d} \qquad \text{(S8)}$$

In Eq. S8 $s_{\bar{\sigma}_{E,X}}$ is the SEM in the absorption cross section of element X at photon energy *E*, $s_{\bar{A},E}$ is the SEM in the absorption at energy *E* (as given by Eq. S7), ρ_X is the elemental density of element X (in mol cm^{-3}) and *d* is the sample thickness. Elemental density was calculated using reference values for the compounds (ρ = 1.00 g cm^{-3} for polystyrene, 1.19 g cm^{-3} for polymethyl methacrylate, 7.27 g cm^{-3} for tin) and the molar mass of the monomer (polymers) or atomic weight (tin). The errors in the density and thickness were neglected here. The thus obtained values for $s_{\bar{\sigma}_{E,X}}$ were used to calculate contributions of these values to the error in elemental composition, making use of the propagation of errors formula Eq. S5.

STXM reference measurements. To check the feasibility of our approach, Eq. S4 was first used to measure elemental concentrations of an unexposed TinOH film. A partially developed TinOH film was used for this, containing both the unexposed film (~26 nm) and bare silicon nitride. As a first try, we used tabulated values by Henke and coworkers for the absorption cross sections $\sigma_{X,E}$. The resulting elemental densities are shown in Fig. S3.

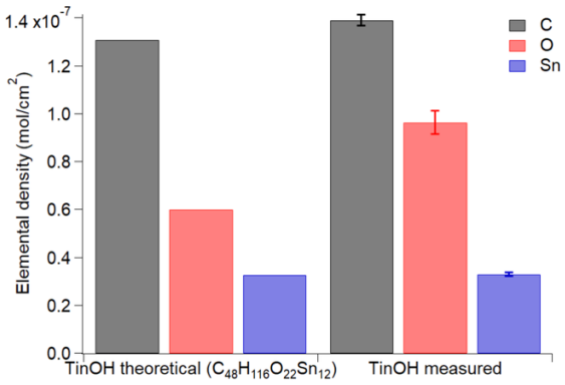

Fig. S3. Bar chart of the theoretical elemental composition (left, as calculated using the molecular formula) and the measured elemental composition (right) as measured using STXM. For the absorption coefficients $\sigma_{X,E}$, values were calculated by interpolation of values obtained from Henke and coworkers.[14] Error bars are the standard error of the mean (SEM). The theoretical composition was normalized to the amount of tin in the experimental composition.

Clearly, the measured elemental composition does not match well with the theoretical one, especially for oxygen. The calculated elemental composition was found to be highly dependent on the exact values for the absorption cross sections. According to Chantler,[13] errors in such values can be 50 – 100%. Therefore, we performed reference measurements on compounds that have a known elemental composition: polystyrene (PS), polymethyl methacrylate (PMMA) and tin (Sn). The elemental absorption coefficients can be expressed as:

$$\sigma_C = \frac{A_{PS}}{d_{PS} \cdot \rho_{C,PS}} \qquad \text{(S9A)}$$

$$\sigma_O = \frac{A_{PMMA} - A_{PMMA(carbon)}}{d_{PMMA} \cdot \rho_{O,PMMA}} \qquad \text{(S9B)}$$

$$\sigma_{Sn} = \frac{A_{Sn}}{\rho_{Sn} \cdot d_{Sn}} \qquad \text{(S9C)}$$

In Eq. S9, A_{PS} is the absorption of the polystyrene flake, d is the flake thickness in cm, and $\rho_{C,PS}$ is the density of carbon in PS in mol cm^{-3}. This is given by (ρ_{PS}/MW_S) × 8, in which ρ_{PS} is the density of polystyrene in g cm^{-3}, MW_S is the molecular weight of styrene in g mol^{-1}, and 8 is the number of carbon atoms in a styrene monomer. For the PMMA measurement on oxygen, the absorption is obtained by subtracting the absorption that is induced by carbon ($A_{PMMA\ (carbon)}$), given by $\rho_C \rho_{C,PMMA} d_{PMMA}$, from the total absorption. For PS and PMMA, a small correction for the absorption of hydrogen was applied by using tabulated values by Henke et al.[14]

The quality of the PS and PMMA samples was studied by measuring carbon K-edge spectra (see Fig. S4). A good agreement with literature spectra was found.[16, 17] The absorption cross section predicted by the tabulated data at 320 nm agree very well with the experimental result.

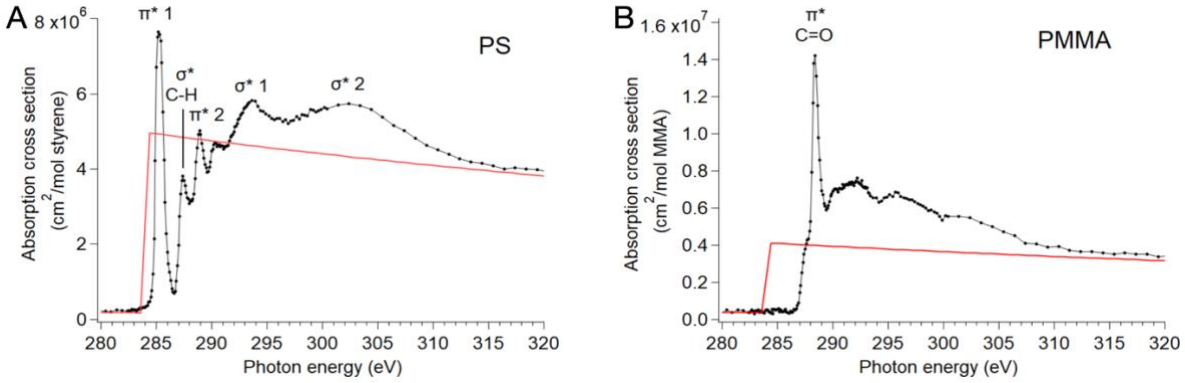

Fig. S4. Carbon K-edge spectra of (a) polystyrene (240 nm) and (b) polymethyl methacrylate films (77 nm). The absorption coefficient is calculated in cm^2 per mol of the monomer (styrene, methyl methacrylate). The red lines show the spectra calculated from tabulated values.[14, 18] Peak assignments are based on refs. [16] and [19] for PS and refs. [17] and [20] for PMMA.

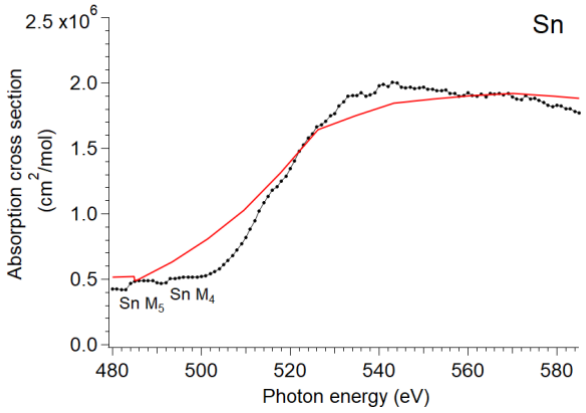

Fig. S5. Experimental $M_{4,5}$-edge spectrum of Sn (flake, thickness ~ 177 nm, β form). This spectrum is an average of three separate measurements. The red line shows the spectrum calculated from tabulated values.[14, 18]

For Sn, the oxygen K-edge and Sn $M_{4,5}$-edges (480 – 590 eV, Fig. S5) were scanned, to study possible contamination with oxygen. Since the Sn sample was briefly exposed to air, formation of an oxide layer on the surface is probable. As is known from previous studies, tin is not oxidized rapidly under ambient conditions and forms only a thin layer of tin (II) oxide,[21] of which the thickness is negligible compared to the total sample thickness. For comparison, spectra obtained from tabulated values were additionally plotted. In this range, both the $M_{4,5}$-edges of tin (very broad, with two weak pre-edge resonances at low photon energies) and oxygen K-edge (sharp resonances around 540 eV) are present. Elemental tin, tin (II) oxide (SnO) and tin (IV) oxide (SnO_2) were all studied previously by others using Electron Energy Loss Spectroscopy (EELS).[22, 23] A distinct resonance was shown to be present for SnO between 535 and 540 eV. Although some weak features can be observed in this region, clearly the SnO contribution to the experimental spectrum is small. Therefore, we assumed only a very thin (3 nm) layer of SnO on both sides of the Sn flake, in line with previous results of tin oxidation at ambient temperature.[21]

The thus obtained values of the cross sections compared to the tabulated values are listed in Table S1.

Table S1. Cross sections (10^5 cm^2 mol^{-1}) of C, O and Sn at selected energies. Tabulated (Tab.) values from Ref. [14].

Photon energy (eV)		σ_C	σ_O	σ_{Sn}
320	Tab.	4.77	0.67	7.93
	Exp.	4.97 ± 0.2%	1.09 ± 5%	7.60 ± 0.7%
515	Tab.	1.53	0.20	12.1
	Exp.	1.58 ± 0.3%	0.13 ± 20%	11.7 ± 0.3%
550	Tab.	1.29	3.31	18.7
	Exp.	1.32 ± 0.7%	4.12 ± 1.4%	20.1 ± 0.4%

The absorption cross sections are close to the tabulated values, but they do not completely match them. The reason could be either experimental error or shortcomings of the tabulated values. The main difference is in the oxygen absorption coefficient at 515 eV, which was measured to be ~1.6× lower. This value was obtained from the reference measurement on PMMA, subtracting absorption caused by carbon from the total absorption (see Eq. S1). The contribution of oxygen to the absorption is quite small at 515 eV, having both a low absorption cross section and a low elemental density (2.5× lower than carbon). Therefore, this value may be more prone to errors than others, because a small deviation in absorption value already leads to a large deviation in the calculated amount of oxygen as shown by the relatively large error of σ_O at 515 eV.

The elemental composition of TinOH, making use of experimentally obtained elemental absorption coefficients, is shown in Fig. 2A in the main text. As can be seen, the experimental elemental composition matches the theoretical cross section within the error margin. However, for the closely related TinF (Fig. 2B), the experimental data agree less well with the theoretical composition. Clearly, the amount of oxygen has the largest uncertainty, which is a direct result of the absorption coefficient of oxygen having a relatively large error.

RGA measurements: methodology and instrumentation. Outgassing experiments were performed using a tool located in IMEC (Leuven, Belgium).[24-26] The tool includes a (Hamamatsu) Energetiq EQ-10 Z-pinch xenon plasma source for EUV exposure. The EUV radiation from the source is filtered by a Zr spectral purity filter and reflected by a multilayer mirror and grazing incidence mirrors towards the wafer to expose the samples at 92 eV (13.5 nm). The tool is equipped with a Residual Gas analyzer (RGA) consisting of a Pfeiffer QMG422 mass spectrometer which can measure over an atomic mass unit (amu) range of 1 to 512 amu. The beam diameter on the wafer is ~5 mm, with an irradiance of 3 mW cm^{-2}. The thickness of the films was measured using an ellipsometer (KLA-Tencor ASET F5x), and a Cauchy model was used to fit the data.

We performed three types of measurements on the TinOH resist films on silicon wafers:

- Use of the RGA to identify the outgassing molecules from the resist during exposure by recording their mass spectra
- The outgassing rate of particular masses over exposure time was monitored using the RGA fast acquisition scan mode.
- We exposed the sample using the EUV source to different exposure doses, and the corresponding thickness change at each applied dose was measured using ellipsometry before and after development to obtain the contrast curve of the resist.

Mass spectrometry of tin-oxo cage outgassing fragments. For this measurement, a thin layer of TinOH photoresist (~11 nm) was coated on a 4-inch Si wafer. The wafer was inserted into the RGA tool on an x-y stage. The RGA tool operates in a vacuum environment, but gas molecules always penetrate the chambers. Therefore, a mass spectrum was recorded from the gas molecules present inside the tool as the background before starting the exposure, exemplified in Fig. S6. Afterwards, the resist-coated wafer was exposed to the 92 eV beam, with the beam continuously scanning the sample's surface at a fixed scanning speed of 0.5 mm s^{-1}, which is one tenth of the beam diameter. The outgassing data were collected in eleven subsequent exposure cycles. During each exposure, which took ~135 s, a mass spectrum from 1 to 300 amu was recorded from the outgassing resist species, with the sample being exposed to up to ~30 mJ cm^{-2}. This experiment was performed on two independently prepared samples of TinOH, and on one sample of TinF.

In an RGA measurement, outgassing fragmented ions are detected in units of partial pressure (mbar), but they can be converted to molecules cm^{-2} s^{-1} using equation S9.[i,ii]

$$R_i = S_{eff}\frac{P_{res} - P_{bg}}{k_B T A} \qquad \text{(S9)}$$

In eq. S9 R_i is the outgassing rate for a certain mass in molecules cm^{-2} s^{-1}, S_{eff} is the pumping speed, k_B the Boltzmann constant, T is the temperature (290 K), P_{res} and P_{bg} are the partial pressures measured for resist and background, respectively, and A is the area exposed to EUV photons (0.2 cm^2). The pumping speed for this system has been determined experimentally and calibrated to be 258 L s^{-1}. This calibration, however, was not recent and for the present

[i] "Partial pressure measurement in vacuum technology," *Balzers Instruments, FL-9496 Balzers, Liechtenstein,* (1983).

[ii] "Vacuum technology know how," Pfeiffer Vacuum GmbH, (2009).

experiments we cannot rely on this in an absolute sense. The relative outgassing rates are not affected by this.
We used the NIST Mass Spectrometry library as the reference to identify the outgassing molecules in the recorded mass spectrum and estimate each outgassing species' contribution to the recorded spectrum.[27-29] By comparing the RGA outgassing data with those obtained using a witness sample it was previously found that the RGA is less sensitive to lower m/z ions than to ions with higher m/z values,[30] and a calibration based on this finding was used in the present work.

Fast acquisition RGA measurement. Time resolved RGA measurement in the fast acquisition mode with a temporal resolution of ~0.65 s enable us to monitor the outgassing rate of four selected ions over the exposure time. A TinOH film of approximately 24 nm, coated on an 8-inch wafer, was used for these measurements. We selected m/z 56, 84, 44, and 2, representative of butene, octane, carbon dioxide, and hydrogen, respectively.
Fifteen different spots on the wafer were exposed to EUV photons up to different dose values by increasing the exposure time from one spot to the next. Full data for each spot are available in the data repository, but since they were virtually identical we present and discuss only the data for the longest exposure here. (Fig. 6 in the main text).
The background mass spectrum was recorded on each spot before launching the exposure.

Additional experimental results and data analysis

Mass spectrometry of the tin-oxo cage outgassing products

Fig. S6 shows the recorded background spectrum from the gas molecules present inside the tool before the start of the exposure. There is a relatively high background from water molecules (m/z 16 to 19), hindering the detection of any possible outgassing ions from the resist in this range. The second highest peaks in the background belong to the penetrating air into the system with nitrogen and oxygen peaks at m/z 28 and 32, respectively. To be able to visualize the contribution of other masses to the background spectrum which are much smaller than those of water and air, the peaks corresponding to water and air were removed from the background, simply by setting their values equal to zero, and the remaining spectrum is represented in Fig. S6B. In this figure, for instance, peaks from xenon gas (m/z 64 – 68 and 128 – 132) used in the EUV source, carbon dioxide (m/z 12 and 44), hydrogen (m/z 1 and 2) could be observed in the background as well.

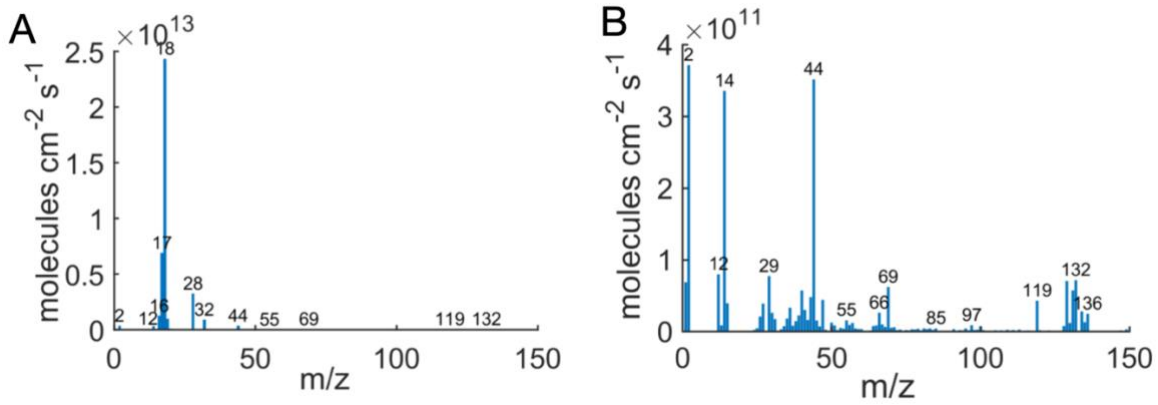

Fig. S6. Example of a background spectrum in the RGA tool measured before exposing the sample. A. Background spectrum dominated by water (m/z 16-19) and air molecules (m/z 28 and 32); B. Remaining background after removing the peaks from water, nitrogen, and oxygen.

All outgassing spectra recorded by the RGA tool for 11 exposure cycles are averaged together and the result is shown in Fig. S7 after background subtraction. The measured spectrum is plotted just up to 120 amu since no ions from the resist could be detected at higher m/z values. The full data up to 300 amu are available in the data repository at https://doi.org/10.21942/uva.30651692.

Evidently, there is little difference between the two measurents on TinOH and the one on TinF. Comparing the obtained mass spectra in Fig. S7 and the NIST library (Fig. S8), we could identify 1-butene, *n*-butane, *n*-octane, carbon dioxide, and hydrogen as the main outgassing products during the exposure with the corresponding characteristic masses as shown in Table S2.

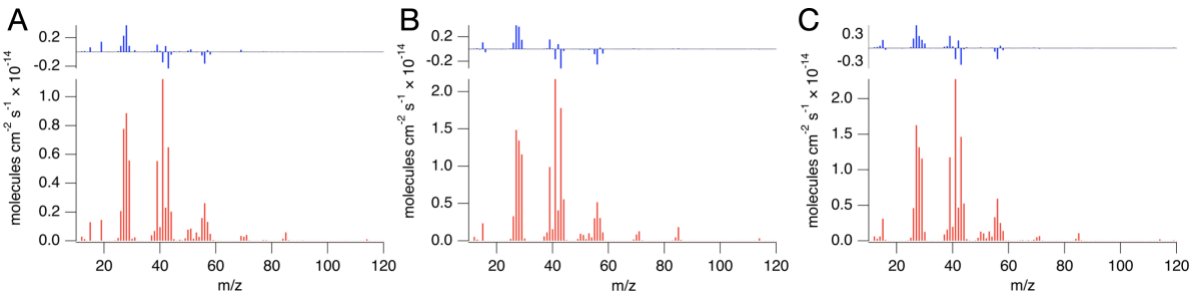

Fig. S7. Outgassing mass spectra averaged over the 11 recorded periods of exposure, after background subtraction. A. TinF B. TinOH run 1 C. TinOH run 2. Residuals of the fit to the sum of contributions of butene, butane, CO_2 and octane are shown above each spectrum in blue.

Table S2. Main outgassing products from tin-oxo cages, with some of the peaks assigned to the outgassing molecules.[27]

Outgassing molecule	characteristic peaks
Octane	69 – 72, 83 – 85, 86, 114 (M^+)
Butene	39, 41, 56 (M^+)
Butane	43, 58 (M^+)
Carbon dioxide	12, 44
Hydrogen	1, 2

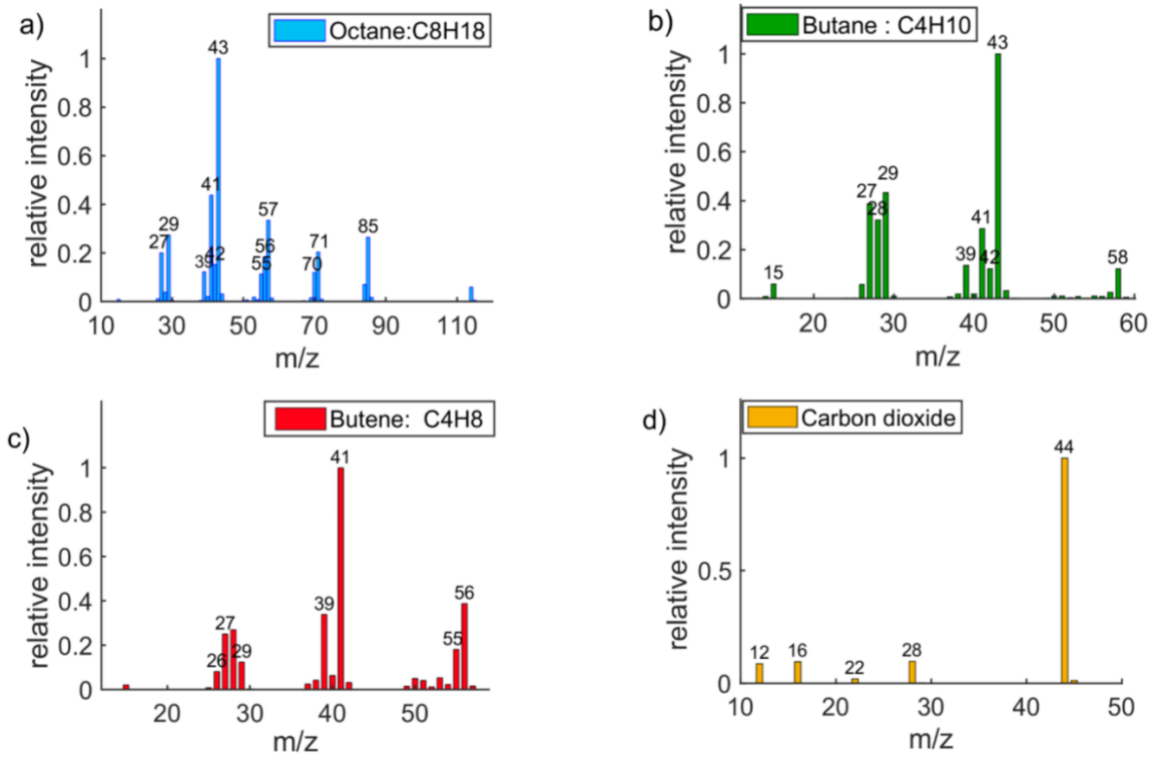

Fig. S8. Mass spectra (electron impact ionization) of the main outgassing compounds from the NIST database.[27]

All outgassing spectra recorded individually per exposure period were summed over the detected ion intensity, and the result is plotted in Fig. S9 in black, showing the outgassing rate of the material measured during each exposure period. Green, red, blue, and orange curves show the calculated contributions from the outgassing butene, butane, octane, and carbon dioxide to the total value, respectively. The black curve is the sum of the contributions from the four outgassing species.

To calculate the contribution of octane to the total measured values, its unique peaks are used that do not overlap with other outgassing species (m/z 71, 72, 84, 85, 86 and 114). The ratio between the measured values and the corresponding one from NIST is calculated. This ratio is then multiplied by the whole octane mass spectrum from NIST, and this is considered as the contribution of octane (blue curve in fig. S9) to the total measured one (black line in Fig. S9). After subtracting the octane spectrum from the total measured one, the remaining spectrum is fitted as a sum of the contributions from butane, butene, and carbon dioxide, respectively, using the NIST reference spectra. Residuals of the fits are shown in Fig. S7. When the entire data sets are fitted as a sum of all four components, large relative errors appear in the peaks of octane at m/z >60 and unrealistically low or even negative outgassing rates are found for octane. As discussed in the main text, several factors may be responsible for the imperfect fit. Since the contribution of octane is much smaller than that of butene and butane, errors in the contributions of the latter two dominate the fit in the low-mass region, leading to the physically unrealistic estimation of the amount of octane when all components are fitted simultaneously.

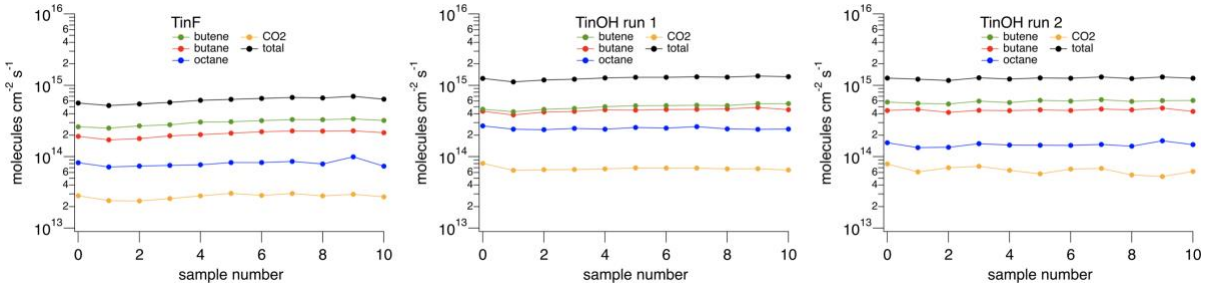

Fig. S9. Calculated contributions from the main outgassing species to the total outgassing rate measured in each exposure period. The circles show the real data from the measurement. The mass spectra were measured in 11 subsequent cycles with the sample being exposed to 30 mJ cm^{-2} during each measurement.

Film thickness evolution as a function of exposure dose

To determine how the thickness of the resist film changes with exposure dose, 16 different spots were exposed to different EUV doses on a TinOH coated 8-inch Si wafer. The thickness change at each of these spots was measured using ellipsometry before and after exposure. The initial film thickness (before exposure) at these 16 spots was found to be 23.3 nm on average. Then the film was developed, and the corresponding induced thickness change was measured at the same spots and analyzed using the same Cauchy model. The results are shown in Fig. S10.

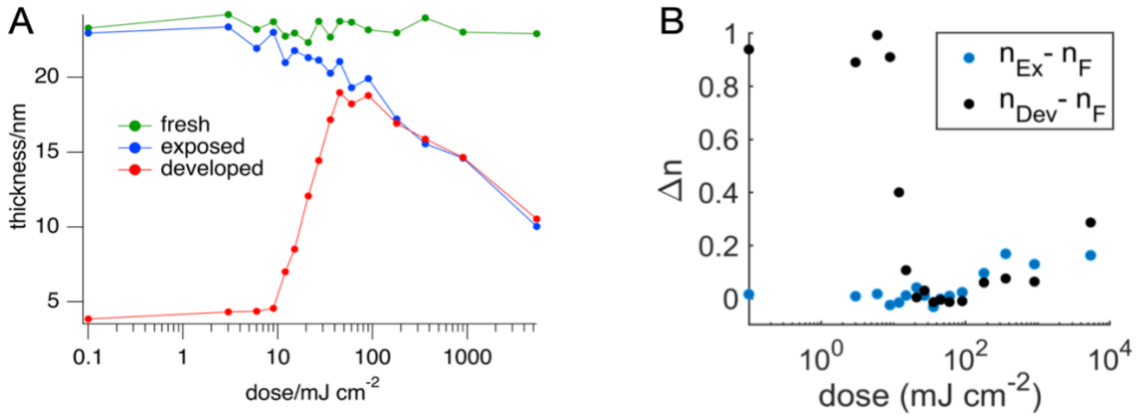

Fig. S10. A. Results of ellipsometry measurement of thickness of TinOH resist film measured at 16 different positions with different exposure doses, before exposing the wafer, after exposure to EUV, and after development. B. Differences between the refractive indices measured on the same spots for the fresh film (n_F = 1.62 $\pm$ 0.2), after the exposure (n_{Ex}) and after development (n_{Dev}).

From Fig. S10A, it would appear that the unexposed resist could not be completely removed at the lowest doses, in contrast with earlier observations.[6] The reason for this apparent discrepancy becomes clear when we look at the relative difference (Δn) between the fresh film's refractive indices (n_F) and those measured on the same spots after exposure (n_{Ex}) and after development (n_{Dev}), as presented in Fig. S10B. The ellipsometry was performed over a broad wavelength range from 300 to 750 nm, and the refractive indices are reported at 633 nm. The fitting model for the thicknesses in Fig. S10 simply considers of a resist layer on top of an infinite silicon layer. Thus, it ignores the presence of native oxide on the wafer and the HMDS coating. Therefore, the large Δn values (n_{Dev} - n_F) for doses between 0 and 9 mJ cm^{-2}

can be attributed to the presence of HMDS and SiO_2; the resist has actually been washed away, and the apparent 4 nm initial thickness for the developed film can be safely ignored. This implies, however, that the same correction needs to be made to the thickness measurement of the unexposed and exposed areas. Therefore in Fig. 7A in the main text a background of 4 nm was subtracted from the data in Fig. S10A.

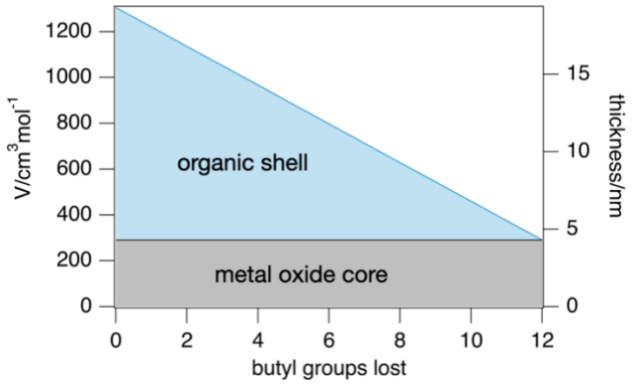

Fig. S11. Schematic representation of shrinkage model.

We observed (Fig. S10 and Fig. 7B) that the thickness of the resist with exposure gradually decreases, with ~2.7 nm reduction occurring at the dose needed for full condensation (45 mJ cm^{-2}). This thickness change is attributed to the escape of the butyl groups from the resist structure, leading to the gradual shrinkage of the resist with exposure.
Assuming that at full exposure all 12 butyls and all volatile molecules of water are dissociated from the cage structure, the final product would have the stoichiometry Sn_2O_3, which has a density of 5.9 g cm^{-3}.[31]

The density of TinOH crystals has been reported as 1.839 g cm^{-3}, giving a molecular volume of 1474 cm^3 mol^{-1}.[32] It is known, however, that the TinOH crystals easily lose the co-crystallized isopropanol.[32] Our computational model for TinOH has the isopropanol molecules replaced by water.[33] The computed volume of this is 89% of that of the X-ray structure, giving an estimated density of 1.947 g cm^{-3} and a volume of 1305 cm^3 mol^{-1}. The final inorganic product has the composition $Sn_{12}O_{18}$ and a volume 290 cm^3 mol^{-1}, which is 22% of the original volume. If we assume a linear shrinkage with conversion, graphically illustrated in Fig. S11, we find that the thickness loss of 2.7 nm at the dose of maximum film thickness (45 mJ cm^{-2}) corresponds to a loss of 2.16 butyl groups per TinOH molecule.
From the density ρ, the molecular weight M and the film thickness d = 19.3 nm we calculated the molecular surface density S as $S = \rho d/M = 8.903 \times 10^{14}$ molecules cm^{-2}. The absorbed photon flux is given by the product of the dose (45 mJ cm^{-2} corresponds to $N_{ph} = 3.053 \times 10^{15}$ photons cm^{-2}) and the fraction of photons absorbed: $f = 1 - e^{-\alpha d} = 0.19$, where $\alpha = 10.9$ μm^{-1} is the absorption factor.[34] The average quantum yield of butyl loss over the 45 mJ dose is then $2.16 \times S/fN_{ph} = 3.3$.

Computational results

For a computational estimation of the reaction energies shown in Scheme 1, structures were optimized using the B3LYP functional with the LANL2DZ basis set, using the Gaussian program.[35] At the same level, the zero-point energies were evaluated, and single point

energies for calculation of the reaction energies were obtained using the Def2TZVP basis set. Table S3 lists all results. The structures are provided in xyz format in a plain text file, and as individual files in the data repository at https://doi.org/10.21942/uva.30651692. Some results were published in ref. [33] and are included here for completeness.

The model of TinOH includes 4 water molecules to provide a stabilizing environment for the basic and nucleophilic OH^- ion, similar to the isopropanol molecules in the TinOH crystal structure (Fig. S12A).

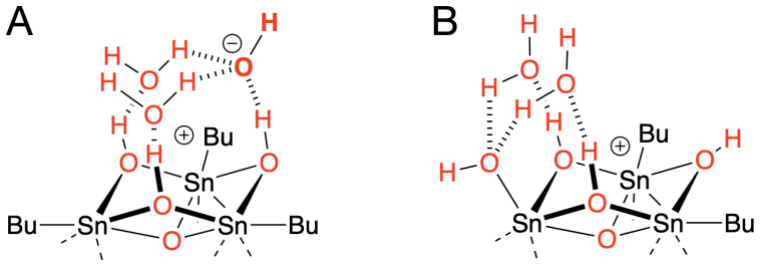

Fig. S12. A. Hydrogen bonding pattern in the computational TinOH model with 4 water molecules, shown for one of the two "cap" regions of the molecule, with the three six-coordinated tin atoms. B. Stable product after ionization, butyl loss, and rearrangement of the bonding pattern in the cap region.

Table S3. Computed energies and zero-point vibrational energies of TinOH and its products.

species	E(LANL2DZ)[a]	E(Def2-TZVP)[b]	ZPE[c]
butyl radical	-157.76248	-157.84813	0.11738
butene	-157.19789	-157.28458	0.10906
butane	-158.43230	-158.51984	0.13265
octane	-315.65928	-315.83152	0.24690
$SnBu_{12}$ neutral	-3901.62210	-6434.76458	1.74597
$SnBu_{12}$ cation radical	-3901.36962	-6434.51232	1.74545
$SnBu_{12}$ anion radical	-3901.63239	-6434.81184	1.73821
$SnBu_{11}$ neutral radical	-3743.75511	-6276.82668	1.62239
$SnBu_{11}$ cation	-3743.63780	-6276.69278	1.62625
$SnBu_{11}$ anion	-3743.87670	-6276.97020	1.62092
$SnBu_{11}CH_2CH•Et$	-3900.96445	-6434.10695	1.73182
$SnBu_{10}$	-3585.91979	-6118.93550	1.49808

[a] geometry optimized with B3LYP/LANL2DZ. [b] single point energy B3LYP/Def2-TZVP//B3LYP/LANL2DZ. [c] zero-point vibrational energies B3LYP/LANL2DZ.

The 12 butyl groups are oriented in a relatively favorable manner but no attempt was made to find the absolute lowest-energy conformation, which may be different in the different reaction products, because this would be tedious and unnecessary.

Geometry optimization of the TinOH radical cation leads to substantial lengthening of the Sn-C bond of one of the six-coordinated Sn atoms in the "cap" region of the cage. Upon removal of the butyl group, forming the $Sn_{12}Bu_{11}$ cation, moving the OH^- anion towards the unsaturated Sn atom, and optimization, an Sn-OH bond was formed, as shown in Figure S12B.

In the TinOH radical anion, the singly occupied molecular orbital is delocalized on the central belt region, and all Sn-C bonds are only slightly lengthened. The most stable $Sn_{12}Bu_{11}$ anion is obtained by removing one of the butyl groups on the five-coordinated Sn atoms.
When a butyl radical abstracts a hydrogen atom from a neighboring cage, an $Sn_{12}Bu_{11}$-CH_2-$HC^{\bullet}$-Et radical can be formed, which can fragment to butene plus the tin-centered radical $Sn_{12}Bu_{11}^{\bullet}$. This is the same species that is formed by homolytic bond cleavage of an Sn-C bond, which is the primary photochemical reaction of tin cages induced by UV light.[36] The same radical is formed when a butyl radical attacks an Sn-C bond of the intact tin cage. Of course, the same reactions can also occur with the $Sn_{12}Bu_{11}$ anion or cation instead of the pristine $Sn_{12}Bu_{12}$ cage, but these options were left for later investigation.

Author Contributions

Table S4. Author contributions following the CRediT taxonomy.

	Conceptualization	Data curation	Formal Analysis	Funding acquisition	Investigation	Methodology	Project administration	Resources	Software	Supervision	Validation	Visualization	Writing – original draft	Writing – review & editing
Najmeh Sadegh	■	■	■		■							■	■	■
Jarich Haitjema	■	■	■		■			■	■		■	■	■	■
Yu Zhang			■		■								■	■
Dimitrios Kazazis						■	■							■
Michaela Vockenhuber					■	■	■	■			■			■
Yasin Ekinci				■		■		■		■				■
Lianjia Wu					■									■
Olivier Lugier					■									■
Ivan Bespalov					■									■
Ivan Pollentier		■	■	■	■	■		■						■
Danilo De Simone				■			■			■				■
Katharina Witte					■	■								■
Benjamin Watts				■	■	■	■	■	■					■
Albert M. Brouwer	■	■	■	■	■		■		■	■	■	■	■	■

References

1 B. Cardineau, R. Del Re, M. Marnell, H. Al-Mashat, M. Vockenhuber, Y. Ekinci, C. Sarma, D. A. Freedman and R. L. Brainard. Photolithographic properties of tin-oxo clusters using extreme ultraviolet light (13.5 nm). *Microelectron. Eng.,* 2014, **127**, 44-50. doi:10.1016/j.mee.2014.04.024

2 C. Eychenne-Baron, F. Ribot and C. Sanchez. New synthesis of the nanobuilding block $\{(BuSn)_{12}O_{14}(OH)_6\}^{2+}$and exchange properties of $\{(BuSn)_{12}O_{14}(OH)_6\}(O_3SC_6H_4CH_3)_2$. *J. Organomet. Chem.,* 1998, **567**, 137-142. doi:10.1016/S0022-328X(98)00676-7

3 L. Van Lokeren, R. Willem, D. van der Beek, P. Davidson, G. A. Morris and F. Ribot. Probing the Anions Mediated Associative Behavior of Tin-12 Oxo-Macrocations by Pulsed Field Gradient NMR Spectroscopy. *J. Phys. Chem. C,* 2010, **114**, 16087-16091. doi:10.1021/jp100709j

4 Y. Zhang, J. Haitjema, S. Castellanos, O. Lugier, N. Sadegh, R. Ovsyannikov, E. Giangrisostomi, F. O. L. Johansson, E. Berggren, A. Lindblad and A. M. Brouwer. Extreme ultraviolet photoemission of a tin-based photoresist. *Appl. Phys. Lett.,* 2021, **118**, 171903. doi:10.1063/5.0047269

5 D. Nečas and P. Klapetek. Gwyddion: an open-source software for SPM data analysis. *Centr. Eur. J. Phys.,* 2012, **10**, 181-188. doi:10.2478/s11534-011-0096-2

6 J. Haitjema, Y. Zhang, M. Vockenhuber, D. Kazazis, Y. Ekinci and A. M. Brouwer. Extreme ultraviolet patterning of tin-oxo cages. *J. Micro/Nanolitho., MEMS, MOEMS,* 2017, **16**, 033510. doi:10.1117/1.JMM.16.3.033510

7 J. Raabe, G. Tzvetkov, U. Flechsig, M. Böge, A. Jaggi, B. Sarafimov, M. G. Vernooij, T. Huthwelker, H. Ade, D. Kilcoyne, T. Tyliszczak, R. H. Fink and C. Quitmann. PolLux: a new facility for soft x-ray spectromicroscopy at the Swiss Light Source. *Rev. Sci. Instrum.,* 2008, **79**, 113704. doi:10.1063/1.3021472

8 L. Wu, I. Bespalov, K. Witte, O. Lugier, J. Haitjema, M. Vockenhuber, Y. Ekinci, B. Watts, A. M. Brouwer and S. Castellanos. Unravelling the effect of fluorinated ligands in hybrid EUV photoresists by X-ray spectroscopy. *J. Mater. Chem. C,* 2020, **8**, 14757-14765. doi:10.1039/d0tc03216f

9 N. Thakur, M. Vockenhuber, Y. Ekinci, B. Watts, A. Giglia, N. Mahne, S. Nannarone, S. Castellanos and A. M. Brouwer. Fluorine-Rich Zinc Oxoclusters as Extreme Ultraviolet Photoresists: Chemical Reactions and Lithography Performance. *ACS Materials Au,* 2022, **2**, 343-355. doi:10.1021/acsmaterialsau.1c00059

10 J. Haitjema, S. Castellanos, O. Lugier, I. Bespalov, R. Lindblad, M. Timm, C. Bülow, V. Zamudio-Bayer, J. T. Lau, B. von Issendorff, R. Hoekstra, K. Witte, B. Watts, T. Schlathölter and A. M. Brouwer. Soft X-Ray Absorption and Fragmentation of Tin-oxo Cage Photoresists. *Phys. Chem. Chem. Phys.,* 2024, **26**, 5986-5998. doi:10.1039/d3cp05428d

11 N. Mojarad, M. Hojeij, L. Wang, J. Gobrecht and Y. Ekinci. Single-digit-resolution nanopatterning with extreme ultraviolet light for the 2.5 nm technology node and beyond. *Nanoscale,* 2015, **7**, 4031-4037. doi:10.1039/C4NR07420C

12 C. T. Chantler. Theoretical Form Factor, Attenuation, and Scattering Tabulation for Z=1–92 from E=1–10 eV to E=0.4–1.0 MeV. *J. Phys. Chem. Ref. Data,* 1995, **24**, 71-643. doi:10.1063/1.555974

13 C. T. Chantler. Detailed Tabulation of Atomic Form Factors, Photoelectric Absorption and Scattering Cross Section, and Mass Attenuation Coefficients in the Vicinity of

Absorption Edges in the Soft X-Ray (Z=30–36, Z=60–89, E=0.1 keV–10 keV), Addressing Convergence Issues of Earlier Work. *J. Phys. Chem. Ref. Data,* 2000, **29**, 597-1056. doi:10.1063/1.1321055

14 B. L. Henke, E. M. Gullikson and J. C. Davis. X-ray interactions: photoabsorption, scattering, transmission and reflection at E = 50-30,000 eV, Z = 1-92. *At. Data Nucl. Data Tables,* 1993, **55**, 181-342. doi:10.1006/adnd.1993.1013

15 H. H. Ku. Notes on the use of propagation of error formulas. *J. Res. Natl. Bur. Stand.,* 1966, **70C**, 263-273.

16 D. A. Outka and J. Stöhr. Curve fitting analysis of near-edge core excitation spectra of free, adsorbed, and polymeric molecules. *J. Chem. Phys.,* 1988, **88**, 3539-3554. doi:10.1063/1.453902

17 J. Wang, H. D. Stöver, A. P. Hitchcock and T. Tyliszczak. Chemically selective soft X-ray patterning of polymers. *J. Synchrotron Radiat.,* 2007, **14**, 181-190. doi:10.1107/S0909049506053829

18 https://henke.lbl.gov/optical_constants/, June 21, 2024.

19 R. J. Klein, D. A. Fischer and J. L. Lenhart. Systematic oxidation of polystyrene by ultraviolet-ozone, characterized by near-edge X-ray absorption fine structure and contact angle. *Langmuir,* 2008, **24**, 8187-8197. doi:10.1021/la800134u

20 X. Zhang, C. Jacobsen, S. Lindaas and S. Williams. Exposure strategies for polymethyl methacrylate from in situ x-ray absorption near edge structure spectroscopy. *J. Vac. Sci. Technol. B,* 1995, **13**, 1477-1483. doi:10.1116/1.588175

21 S. Cho, J. Yu, S. K. Kang and D.-Y. Shih. Oxidation study of pure tin and its alloys via electrochemical reduction analysis. *J. Electron. Mater.,* 2005, **34**, 635-642. doi:10.1007/s11664-005-0077-6

22 H. Lorenz, Q. Zhao, S. Turner, O. I. Lebedev, G. Van Tendeloo, B. Klötzer, C. Rameshan and S. Penner. Preparation and structural characterization of SnO_2 and GeO_2 methanol steam reforming thin film model catalysts by (HR)TEM. *Mater. Chem. Phys.,* 2010, **122**, 623-629. doi:10.1016/j.matchemphys.2010.03.057

23 M. S. Moreno, R. F. Egerton, J. J. Rehr and P. A. Midgley. Electronic structure of tin oxides by electron energy loss spectroscopy and real-space multiple scattering calculations. *Phys. Rev. B,* 2005, **71**, 035103. doi:10.1103/physrevb.71.035103

24 I. Pollentier, G. Aksenov, A. M. Goethals, R. Gronheid, R. Jonckheere and M. Leeson. Measurement and analysis of EUV photoresist related outgassing and contamination. *Proc. SPIE,* 2009, **7271**, 727146-727141. doi:10.1117/12.814862

25 I. Pollentier. Study of EUV Resist Outgassing/Contamination for Device Integration using EUVL Processes. *J. Photopolym. Sci. Technol.,* 2010, **23**, 605-612. doi:10.2494/photopolymer.23.605

26 I. Pollentier, A. T. Venkata and R. Gronheid. Relationship between resist outgassing and EUV witness sample contamination in NXE outgas qualification using electrons and EUV photons. *Proc. SPIE,* 2014, **9048**, 90481B. doi:10.1117/12.2047380

27 P. J. Linstrom and W. G. Mallard. The NIST Chemistry WebBook: A chemical data resource on the internet. *J. Chem. Eng. Data,* 2001, **46**, 1059-1063. doi:10.1021/je000236i

28 P. Ausloos, C. L. Clifton, S. G. Lias, A. I. Mikaya, S. E. Stein, D. V. Tchekhovskoi, O. D. Sparkman, V. Zaikin and D. Zhu. The critical evaluation of a comprehensive mass spectral library. *J. Am. Soc. Mass Spectrom.,* 1999, **10**, 287-299. doi:10.1016/S1044-0305(98)00159-7

29 S. Stein. Mass spectral reference libraries: an ever-expanding resource for chemical identification. *Anal. Chem.,* 2012, **84**, 7274-7282. doi:10.1021/ac301205z
30 I. Pollentier, R. Lokasani, R. Gronheid, S. Hill, C. Tarrio and T. Lucatorto. Relationship between resist related outgassing and witness sample contamination in the NXE outgas qualification using electrons and EUV. *Proc. SPIE,* 2013, **8679**, 86790K. doi:10.1117/12.2011541
31 G. Murken and M. Trömel. Uber das bei der Disproportionierung von SnO entstehende Zinnoxid, Sn_2O_3. *Z. Anorg. Allg. Chem.,* 1973, **397**, 117-126. doi:10.1002/zaac.19733970204
32 F. Banse, F. Ribot, P. Tolédano, J. Maquet and C. Sanchez. Hydrolysis of Monobutyltin Trialkoxides: Synthesis and Characterizations of $\{(BuSn)_{12}O_{14}(OH)_6\}(OH)_2$. *Inorg. Chem.,* 1995, **34**, 6371-6379. doi:10.1021/ic00129a023
33 I. Bespalov, Y. Zhang, J. Haitjema, R. M. Tromp, S. J. van der Molen, A. M. Brouwer, J. Jobst and S. Castellanos. Key Role of Very Low Energy Electrons in Tin-based Molecular Resists for Extreme Ultraviolet Nanolithography. *ACS Appl. Mater. Interfaces,* 2020, **12**, 9881-9889. doi:10.1021/acsami.9b19004
34 R. Fallica, J. Haitjema, L. Wu, S. Castellanos, A. M. Brouwer and Y. Ekinci. Absorption coefficient of metal-containing photoresists in the extreme ultraviolet. *J. Micro/Nanolitho., MEMS, MOEMS,* 2018, **17**, 023505. doi:10.1117/1.JMM.17.2.023505
35 M. J. Frisch, G. W. Trucks, H. B. Schlegel, G. E. Scuseria, M. A. Robb, J. R. Cheeseman, G. Scalmani, V. Barone, G. A. Petersson, H. Nakatsuji, X. Li, M. Caricato, A. V. Marenich, J. Bloino, B. G. Janesko, R. Gomperts, B. Mennucci, H. P. Hratchian, J. V. Ortiz, A. F. Izmaylov, J. L. Sonnenberg, D. Williams-Young, F. Ding, F. Lipparini, F. Egidi, J. Goings, B. Peng, A. Petrone, T. Henderson, D. Ranasinghe, V. G. Zakrzewski, J. Gao, N. Rega, G. Zheng, W. Liang, M. Hada, M. Ehara, K. Toyota, R. Fukuda, J. Hasegawa, M. Ishida, T. Nakajima, Y. Honda, O. Kitao, H. Nakai, T. Vreven, K. Throssell, J. A. Montgomery, Jr., J. E. Peralta, F. Ogliaro, M. J. Bearpark, J. J. Heyd, E. N. Brothers, K. N. Kudin, V. N. Staroverov, T. A. Keith, R. Kobayashi, J. Normand, K. Raghavachari, A. P. Rendell, J. C. Burant, S. S. Iyengar, J. Tomasi, M. Cossi, J. M. Millam, M. Klene, C. Adamo, R. Cammi, J. W. Ochterski, R. L. Martin, K. Morokuma, O. Farkas, J. B. Foresman and D. J. Fox, *Gaussian 16 Revision C.02*, Gaussian, Inc, Wallingford CT, 2016
36 J. Haitjema, L. Wu, A. Giuliani, L. Nahon, S. Castellanos and A. M. Brouwer. UV and VUV-induced fragmentation of tin-oxo cage ions. *Phys.Chem.Chem.Phys.,* 2021, **23**, 20909-20918. doi:10.1039/D1CP03148A